MATERIALS CHEMISTRY FRONTIERS

RESEARCH ARTICLE

View Article Online
View Journal | View Issue

Cite this: *Mater. Chem. Front.*, 2021, **5**, 6883

Facial synthesis of two-dimensional $In_2S_3/Ti_3C_2T_x$ heterostructures with boosted photoactivity for the hydrogenation of nitroaromatic compounds†

Yisong Zhu,[a] Guanshun Xie,[a] Guohao Li,[a] Fei Song,[a] Changqiang Yu,[a] Zhenjun Wu,*[b] Xiuqiang Xie *[a] and Nan Zhang *[a]

Received 12th June 2021,
Accepted 17th July 2021

DOI: 10.1039/d1qm00844g

rsc.li/frontiers-materials

Two-dimensional (2D) heterostructures have gained increased interest in recent years due to the integrated functionalities of the individual building blocks and beyond. Herein, we have fabricated 2D $In_2S_3/Ti_3C_2T_x$ heterostructures through a facile one-step low temperature refluxing method. While bare In_2S_3 tends to evolve as nanoparticles, it is found that $Ti_3C_2T_x$ (MXene) acts as the platform for directing the growth of 2D In_2S_3 nanoflakes, thereby generating 2D $In_2S_3/Ti_3C_2T_x$ heterostructures. For the probe reaction of nitroaromatic compound hydrogenation, $In_2S_3/Ti_3C_2T_x$ composites exhibited boosted photocatalytic activities compared to bare In_2S_3, which can be ascribed to the favorable active site exposure in the 2D/2D heterostructures and the "electron sink" effect of the $Ti_3C_2T_x$ nanosheets. This work distinctly indicates that $Ti_3C_2T_x$ nanosheets are a promising platform for fabricating 2D/2D heterostructures for photoredox catalysis.

1. Introduction

As one of the effective ways to relieve the increasingly serious problems of environmental pollution and energy crisis, semiconductor-based photocatalysis has recently aroused tremendous research interest.[1–5] However, there are still many scientific problems to be solved in the photocatalytic technology, such as the high electron–hole recombination rate and insufficient surface active-site exposure for photocatalysis, which greatly limit photocatalytic activity.[6–8] In recent years, tremendous efforts have been applied to design effective semiconductor photocatalysts. Among numerous strategies for improving photocatalytic activity, coupling semiconductors with a cocatalyst to form 2D/2D heterostructures holds great superiority over 0D/2D and 1D/2D heterostructures.[9] The 2D/2D heterostructures afford more conducive carrier transfer channels and greater contact area,[10–12] which are beneficial to achieve improved photocatalytic activity. At present, many reported 2D-2D heterostructures exhibit improved photocatalytic activity, such as MXene/Bi_2WO_6,[13] $BiVO_4/Ti_3C_2$,[11] $Zn_3In_2S_6$/FCN,[14] BiOBr/$La_2Ti_2O_7$,[15] SnS_2/g-C_3N_4,[16] and rGO/g-C_3N_4.[17] However, there are some bottlenecks of the currently commonly used 2D cocatalysts, such as limited functional groups to establish intimate interfacial interaction with semiconductors, poor conductivity resulting in inefficient separation of charge carries, and lack of hydrophilic functionalities leading to instability in aqueous solution,[18] which make the photocatalytic activity unsatisfactory. Therefore, it remains desirable to explore new 2D materials as cocatalysts to overcome these shortcomings in constructing 2D heterostructured photocatalysts.

$Ti_3C_2T_x$ (T_x stands for the surface terminations, such as –OH, –O and –F), as a typical example in the family of 2D metal carbides/nitrides known as MXene, has attractive properties of metallic conductivity and anisotropic behavior of carrier mobility,[19,20] and has shown great application prospects in energy-related applications.[21–25] In addition, the surface functional groups of $Ti_3C_2T_x$ not only endow it with good dispersion and great anti-aggregation ability in aqueous medium, but also provide anchoring sites for the growth of semiconductors on its surface.[26] Furthermore, high work function and electrical conductivity contribute to the efficient transport of photogenerated electrons and inhibit their recombination with holes, thereby improving the photocatalytic activity of the composites.[27–29] These merits of $Ti_3C_2T_x$ make it a promising co-catalyst for constructing 2D heterostructured photocatalysts.

In this work, $In_2S_3/Ti_3C_2T_x$ composites have been constructed through a facile one-step refluxing method. Intriguingly, it has been found that $Ti_3C_2T_x$ plays an essential role in directing the 2D

[a] College of Materials Science and Engineering, Hunan Joint International Laboratory of Advanced Materials and Technology for Clean Energy, Hunan University, P. R. China. E-mail: xiuqiang_xie@hnu.edu.cn, nanzhang@hnu.edu.cn

[b] College of Chemistry and Chemical Engineering, Hunan University, P. R. China. E-mail: wooawt@hnu.edu.cn

† Electronic supplementary information (ESI) available. See DOI: 10.1039/d1qm00844g

growth of In_2S_3 nanoflakes, resulting in the construction of 2D $In_2S_3/Ti_3C_2T_x$ heterostructures. The underlying mechanism of $Ti_3C_2T_x$-directed growth of In_2S_3 nanoflakes has been further investigated. In addition, $Ti_3C_2T_x$ also serves as an "electron sink", which is responsible for the extraction of photogenerated electrons from semiconductor In_2S_3, thus improving the photocatalytic activity of $In_2S_3/Ti_3C_2T_x$ composites. As compared to bare In_2S_3, the as-obtained $In_2S_3/Ti_3C_2T_x$ composites exhibit improved photocatalytic activity towards the hydrogenation reduction of nitroaromatic compounds under visible light irradiation. Finally, a possible photocatalytic mechanism was proposed to explain the improved photocatalytic activity.

2. Experimental

2.1. Materials

All reagents and solvents were of analytical reagent grade and were used in accordance with information obtained from commercial suppliers. Hydrochloric acid (HCl), indium chloride tetrahydrate ($InCl_3{\cdot}4H_2O$), thioacetamide (C_2H_5NS, TAA), ammonium formate ($HCOONH_4$), potassium persulfate ($K_2S_2O_8$) and 4-nitroaniline ($C_6H_6N_2O_2$) used in the experiments were all obtained from Sinopharm Chemical Reagent Co. The deionized water (DI water) used in the experiments was from local sources.

2.2. Synthesis of $Ti_3C_2T_x$ nanosheets

$Ti_3C_2T_x$ was prepared by selectively etching an Al layer with HF using Ti_3AlC_2 MAX powder as the raw material. The preparation process was as follows: 1 g of LiF was added to 10 mL HCl (9 mol L^{-1}) solution and stirred evenly. The MAX powder was slowly added to the above solution. The mixture was kept at 35 °C for 24 h, and then was washed with deionized water until the pH of the supernatant was above 5. The obtained product was redispersed in deionized water. After ultrasonic treatment in a water bath for 1 h under N_2 flow, the suspension was centrifuged for 1 h, and the dark green supernatant was collected to obtain delaminated $Ti_3C_2T_x$ colloid solution. The concentration of the delaminated $Ti_3C_2T_x$ was determined by filtering a known volume of the supernatant through a Celgard membrane and measuring the weight of the film after drying.

2.3. Synthesis of the $In_2S_3/Ti_3C_2T_x$ composite and bare In_2S_3

The $In_2S_3/Ti_3C_2T_x$ composite was synthesized by a facile one-step refluxing method. A certain volume of $Ti_3C_2T_x$ suspension was dispersed into deionized water by ultrasonication and the total volume was kept as 100 mL. 250 mg of $InCl_3{\cdot}4H_2O$ was added into the above solution along with stirring for 30 min at room temperature. Then 120 mg of TAA was added into the above solution, and stirred for 30 min. The mixture was refluxed for 5 h at 95 °C under a N_2 flow (60 mL min^{-1}). After the reaction, the sample was cooled to room temperature, and washed three times with deionized water. The precipitate was freeze-dried for 24 h to obtain the $In_2S_3/Ti_3C_2T_x$-x% composite, where x (x = 1, 2, and 3) denotes the weight ratios of $Ti_3C_2T_x$. The synthetic process of bare In_2S_3 was consistent with that for the $In_2S_3/Ti_3C_2T_x$ composite except for the addition of $Ti_3C_2T_x$.

2.4. Materials characterization

X-ray diffraction (XRD) measurements were carried out on a Rigaku SmartLab using Ni-filtered Cu Kα radiation at a scan rate of 0.1° s^{-1}. Transmission electron microscopy (TEM) images and elemental mapping results were collected by using Tecnai G2 F20 S-TWIN at an accelerating voltage of 200 kV. Field-emission scanning electron microscopy (FESEM) was used to determine the morphology of the samples on a JSM-6700F spectrophotometer. UV-vis diffuse-reflectance (DRS) spectra were obtained on a UV-2600 UV-vis spectrophotometer equipped with a diffuse-reflectance accessory, in which $BaSO_4$ was employed as a reference. X-ray photoelectron spectroscopy (XPS) measurements were performed using AXIS SUPRA. JW-BK200C equipment was used to determine the nitrogen adsorption–desorption isotherms and the Brunauer–Emmett–Teller (BET) surface areas. Raman spectra were obtained using an inVia-reflex Laser Raman spectrometer. The photo-luminescence (PL) spectra for the samples were analyzed on an Edinburgh Analytical Instrument F900 spectrophotometer with an excitation wavelength of 420 nm. Photoelectrochemical measurements were carried out on a CHI 660E electrochemical station (Shanghai Chenhua) with a three-electrode system consisting of a working electrode, Pt foil counter electrode, and Ag/AgCl reference electrode. The FTO glass was washed in ethanol ultrasonically for 30 minutes and dried at 60 °C. The boundary of FTO glass was protected with scotch tape. The sample slurry was obtained by dispersing 5 mg of samples in 0.5 mL of *N*,*N*-dimethylformamide (DMF) by ultrasonication, which was then coated on the pretreated FTO glass. After drying, the adhesive tape was removed and the uncoated part of the electrode was pasted with epoxy resin. The exposed area of the working electrode was 0.25 cm^2. A 300 W Xe lamp system (PLS-SXE300D, Beijing Perfectlight) equipped with a UV light filter (to cut off light with $\lambda < 420$ nm) was used as the irradiation source. The working electrode was immersed in an aqueous solution of 0.1 M Na_2SO_4. After the visible light was irradiated for 60 s, the light was turned off to monitor the subsequent decay of photovoltage for 50 s, and the open circuit photovoltage decay (OCP) spectrum was obtained. The electrochemical impedance spectroscopy (EIS) and cyclic voltammogram (CV) experiments were conducted in 0.5 M KCl containing 0.01 M $K_3[Fe(CN)_6]$/$K_4[Fe(CN)_6]$ under open-circuit potential conditions. The transient photocurrent response was conducted in 0.2 M Na_2SO_4 aqueous solution without voltage bias under visible light irradiation. The Mott–Schottky (M–S) experiments were obtained in 0.2 M Na_2SO_4 aqueous solution without additive. The contact angle of water droplet on the freestanding membranes of the exfoliated $Ti_3C_2T_x$ nanosheets was measured using a DSA 100 (KRÜSS) instrument to characterize the surface properties.

2.5. Photocatalytic activity tests

The photocatalytic activity of the prepared samples was tested toward the hydrogenation reduction of nitroaromatic compounds at ambient temperature and N_2 atmosphere using a

300 W Xe lamp with a UV light filter (to cut off light with $\lambda < 420$ nm). 40 mg of photocatalyst and 40 mg of ammonium formate as a hole trapping agent were mixed with 40 mL of 4-nitroaniline (10 ppm) in a reaction bottle with a circulating water system and the mixture was stirred in the dark for 1 h to ensure the establishment of the adsorption–desorption equilibrium between the sample and reactants. The whole experimental process was conducted under N_2 bubbling at a flow rate of 60 mL min^{-1}. During the process of the reaction, 2 mL of liquid was collected at a certain time interval and centrifuged to remove the catalyst completely at 8000 rpm. After that, the solution was analyzed using an ultraviolet-visible light (UV-vis) spectrophotometer (Shimadzu, UV-1780). Control experiments were carried out in a similar manner to the above photocatalytic reduction of nitroaromatic compounds except for the addition of active species scavengers.

3. Results and discussion

The synthesis procedure for the $In_2S_3/Ti_3C_2T_x$ composite is illustrated in Fig. 1a. The exfoliated $Ti_3C_2T_x$ nanosheets are mixed with $InCl_3$, during which the In^{3+} cations are adsorbed on the surface of negatively charged $Ti_3C_2T_x$ nanosheets through electrostatic attractions. Then TAA as the sulfur source is added into the above mixture to undergo a refluxing treatment. During this process, TAA is heated to release S^{2-} ions to react with the adsorbed In^{3+} to form In_2S_3 *in situ* grown on the surface of $Ti_3C_2T_x$ nanosheets, thus giving rise to the formation of $In_2S_3/Ti_3C_2T_x$ composites.

The morphology of the as-prepared sample is firstly studied by scanning electron microscopy (SEM). Bare In_2S_3 consists of aggregated nanoparticles (Fig. S1, ESI†). In contrast, well-defined In_2S_3 nanoflakes are observed for the $In_2S_3/Ti_3C_2T_x$-1% composite (Fig. 1b), suggesting that the introduction of $Ti_3C_2T_x$ nanosheets plays a critical role in controlling the growth of In_2S_3 nanoflakes. The microscopic morphology and structure of the $In_2S_3/Ti_3C_2T_x$ composite have been further analyzed by transmission electron microscopy (TEM). Fig. 1c shows a typical TEM image of the $In_2S_3/Ti_3C_2T_x$-1% composite. It can be clearly seen that many small In_2S_3 nanoflakes are attached to the $Ti_3C_2T_x$ nanosheets, which is in accordance with the results of SEM. The high-resolution TEM (HRTEM) image of $In_2S_3/Ti_3C_2T_x$-1% in Fig. 1d reveals the distinguishable interfaces of In_2S_3 nanoparticles with $Ti_3C_2T_x$ nanosheets. The lattice spacing of 0.285 nm is attributed to the (400) crystal plane of the In_2S_3 in $In_2S_3/Ti_3C_2T_x$ composite. The elemental mapping analysis has been performed to further determine the element distribution. The results in Fig. 1e show that the In, S, Ti and C elements are identically distributed in the $In_2S_3/Ti_3C_2T_x$-1% composite. The mapping image of the In element is basically the same as that of the S element, which overlap with the Ti and C elements. These results indicate that In_2S_3 nanoflakes are uniformly grown on $Ti_3C_2T_x$ nanosheets with intimate interfacial interactions, which facilitates the separation and transfer of photogenerated electrons. Contact angle measurements were conducted to explore the hydrophilicity of the $Ti_3C_2T_x$ nanosheets. From Fig. S2 (ESI†), a small contact angle of 39.4° is observed, indicating the preferable hydrophilicity of $Ti_3C_2T_x$, which is important for the role in directing the growth of 2D In_2S_3 nanoflakes. To explore the growth mechanism of In_2S_3 nanoflakes on the $Ti_3C_2T_x$ nanosheets, the effects of $Ti_3C_2T_x$ content and reaction time (t = 1, 4, and 5 h) were systematically studied. As shown in Fig. S3a–c (ESI†), with the increase of refluxing time, In_2S_3 gradually nucleates and grows on the $Ti_3C_2T_x$ surface. When the refluxing time is prolonged to 4 h, the surface of the $Ti_3C_2T_x$ nanosheets gradually become rough, and small In_2S_3 nanoflakes are observed. After 5 h of refluxing, In_2S_3 grew vertically on the surface of the $Ti_3C_2T_x$ nanosheets to form 2D $In_2S_3/Ti_3C_2T_x$ heterostructures. In addition, when the $Ti_3C_2T_x$ content in the $In_2S_3/Ti_3C_2T_x$ composite increases to 5%, In_2S_3 nanoflakes can still be seen (Fig. S3d, ESI†). However, when the content of $Ti_3C_2T_x$ increases to 20% or 30%, In_2S_3 nanoparticles rather than nanoflakes are generated. These controlled experiments indicate that the content of $Ti_3C_2T_x$ plays a significant role in the morphology regulation of In_2S_3. It is reasonable to propose that low content of $Ti_3C_2T_x$ results in a high density of In_2S_3 nuclei, which favors the vertical growth of nanosheets based on the theory that the steric hindrance from adjacent seeds can hinder the in-plane direction growth.[30]

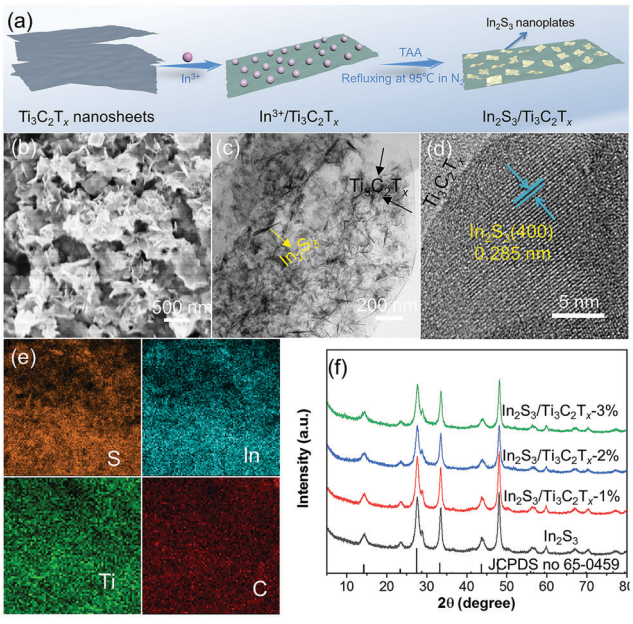

Fig. 1 Illustration of the synthesis process for the $In_2S_3/Ti_3C_2T_x$ composites (a). SEM image (b), TEM image (c), HRTEM image (d), and element mapping (e) of $In_2S_3/Ti_3C_2T_x$-1%. XRD patterns of bare In_2S_3 and $In_2S_3/Ti_3C_2T_x$ composites (f).

X-ray diffraction (XRD) measurements have been conducted to analyze the crystal structure of the as-prepared samples. As demonstrated in Fig. 1f, the characteristic diffraction peaks at 2θ = 14.2, 23.3, 27.4, 28.7, 33.2, 43.6, 47.7, 56.6, 59.4, 66.6 and 69.8° in the XRD spectrum of bare In_2S_3 are indexed to the (111), (220), (311), (222), (400), (511), (440), (622), (444), (731) and (800) crystal planes of the cubic In_2S_3 phase (β-In_2S_3)

(JCPDS no. 65-0459), respectively. The $In_2S_3/Ti_3C_2T_x$ composites exhibit similar XRD patterns to that of bare In_2S_3, demonstrating that the introduction of $Ti_3C_2T_x$ does not change the crystal structure of In_2S_3. Therefore, the possible influence of the crystal structure on the photocatalytic performance of the samples can be eliminated. There are no obvious characteristic diffraction peaks of $Ti_3C_2T_x$ in the XRD patterns, which should be ascribed to the low content of $Ti_3C_2T_x$. In addition, no XRD peaks of TiO_2 can be observed, which clearly indicates that the stability of $Ti_3C_2T_x$ is well sustained. The intensity of the diffraction peaks for In_2S_3 decreases with the increase of $Ti_3C_2T_x$ content in the composites. This should be because the aggregation of In_2S_3 is effectively inhibited by the addition of $Ti_3C_2T_x$ as 2D growing platforms. The composition of the samples has been further confirmed by Raman. As revealed in Fig. S4 (ESI†), the Raman peaks located at 306 cm^{-1} can be associated with the typical vibration modes of β-In_2S_3.[31] As for the $In_2S_3/Ti_3C_2T_x$-1% composite, it is obvious that besides the typical peak of In_2S_3 at 306 cm^{-1}, there is an additional peak centered at 206 cm^{-1}, which can be associated with the vibrations from $Ti_3C_2T_x$.[32] Furthermore, no characteristic peaks of TiO_2 can be seen, which further manifests that $Ti_3C_2T_x$ is well sustained during the fabrication process.

The optical properties of bare In_2S_3 and $In_2S_3/Ti_3C_2T_x$ composites have been studied by UV-vis diffuse reflectance spectra (DRS). As displayed in Fig. S5 (ESI†), the introduction of $Ti_3C_2T_x$ nanosheets leads to the enhanced light absorption of $In_2S_3/Ti_3C_2T_x$ composites in visible light. The absorption gradually increases with the increase of $Ti_3C_2T_x$ content, which could be ascribed to the background light absorption of $Ti_3C_2T_x$. This is consistent with the color of the samples, as shown in the insets of Fig. S5 (ESI†). The above results show that the introduction of $Ti_3C_2T_x$ has a similar effect on the morphology, crystal structure and optical properties of the $In_2S_3/Ti_3C_2T_x$ composites.

The surface chemical states of the as-prepared samples have been analyzed by X-ray photoelectron spectroscopy (XPS). It can be seen from Fig. S6 (ESI†) that In, S, Ti, and C elements are detected in $In_2S_3/Ti_3C_2T_x$-1%, which is consistent with the elemental mapping analysis. In addition, the peak of F element in the survey spectrum of $In_2S_3/Ti_3C_2T_x$-1% is almost extinct compared with bare $Ti_3C_2T_x$, indicating the F element has been exchanged during the refluxing process. In the high-resolution In 3d XPS spectrum of In_2S_3 (Fig. 2a), the binding energies of In 3d at 452.2 eV and 444.7 eV are ascribed to In $3d_{3/2}$ and In $3d_{5/2}$, respectively. Meanwhile, two peaks located at 161.2 eV and 162.3 eV are attributed to S $2p_{3/2}$ and S $2p_{1/2}$ (Fig. 2b).[33] After the introduction of $Ti_3C_2T_x$, the binding energy of In $3d_{3/2}$ and In $3d_{5/2}$ shifted to 452.3 eV and 444.8 eV, while the binding energy of S $2p_{3/2}$ and S $2p_{1/2}$ shifted to 161.3 eV and 162.4 eV, respectively. This implies a decrease in surface electron density of In_2S_3 in the $In_2S_3/Ti_3C_2T_x$-1% composite, suggesting a Schottky effect between the semiconductor In_2S_3 and $Ti_3C_2T_x$, which is favorable for the transfer of photogenerated electrons. As shown in Fig. 2c, there are four peaks located at 281.5 eV, 284.6 eV, 286.5 eV and 288.1 eV, which can be assigned to the Ti–C bond, C–C bond, C–O bond, and C–F bond, respectively.[34]

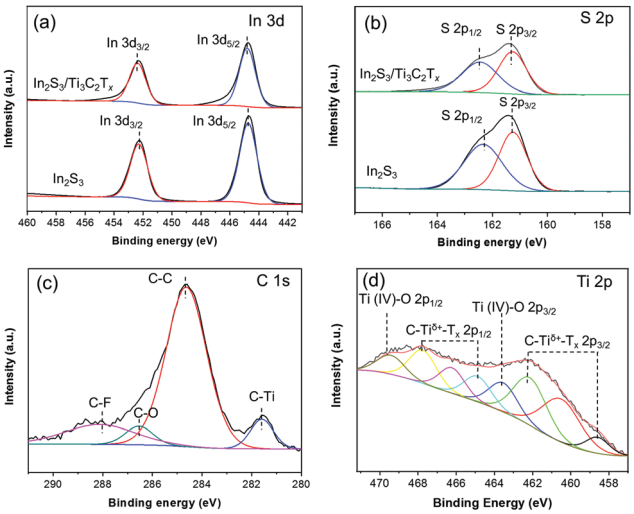

Fig. 2 XPS spectra of In_2S_3 and $In_2S_3/Ti_3C_2T_x$-1%. In 3d (a) and S 2p (b) of In_2S_3 and $In_2S_3/Ti_3C_2T_x$-1%. C 1s (c) and Ti 2p (d) of $In_2S_3/Ti_3C_2T_x$-1%.

As displayed in Fig. 2d, there are four doublets (Ti $2p_{3/2}$–Ti $2p_{1/2}$) in the Ti 2p XPS spectra, three of which correspond to C–Ti^{δ}+–T_x (δ = 1, 2 and 3) while the fourth is attributed to Ti(VI)–O.[35]

The photocatalytic activities of the as-prepared samples have been comparatively evaluated by selective hydrogenation of 4-nitroaniline (4-NA) and other nitroaromatic compounds in water with the addition of ammonium formate as a hole scavenger under visible light irradiation. As shown in Fig. 3a, the conversion of 4-NA reaches 65% over bare In_2S_3 after 140 min. When $Ti_3C_2T_x$ with a weight ratio of 1% is added, the conversion of 4-NA is improved as compared with bare In_2S_3. However, the addition of higher contents of $Ti_3C_2T_x$ (*i.e.*, 2 and 3 wt%) results in a decrease of photocatalytic activity and the $In_2S_3/Ti_3C_2T_x$-3% even exhibits a worse performance than bare In_2S_3. This indicates that an appropriate content of $Ti_3C_2T_x$ combined with In_2S_3 can obtain the optimum photocatalytic activity. With the increase of $Ti_3C_2T_x$ content in the $In_2S_3/Ti_3C_2T_x$ composite, the light through the reaction suspension might be shielded by $Ti_3C_2T_x$ with a dark color, which reduces the effective contact of In_2S_3 nanoflakes with incident photons, and thus leads to a decrease of photocatalytic activity. The transient photocurrent response of the as-prepared samples under intermittent visible light irradiation is shown in Fig. S7 (ESI†). The $In_2S_3/Ti_3C_2T_x$-1% composite exhibits an improved transient photocurrent response compared to bare In_2S_3, indicating the increased transport and separation of photogenerated charge carriers. However, the addition of higher contents of $Ti_3C_2T_x$ (*i.e.*, 2 and 3 wt%) result in the decrease of transient photocurrent response and the $In_2S_3/Ti_3C_2T_x$-3% even exhibits a worse transient photocurrent response than bare In_2S_3. The transient photocurrent response results keep accordance with the above photocatalytic activity results, which further demonstrates an appropriate content of $Ti_3C_2T_x$ combined with In_2S_3 can obtain the optimum photocatalytic activity. The dependence of photoactivity of $In_2S_3/Ti_3C_2T_x$ on the weight ratio of $Ti_3C_2T_x$ has also been found for the hydrogenation of other

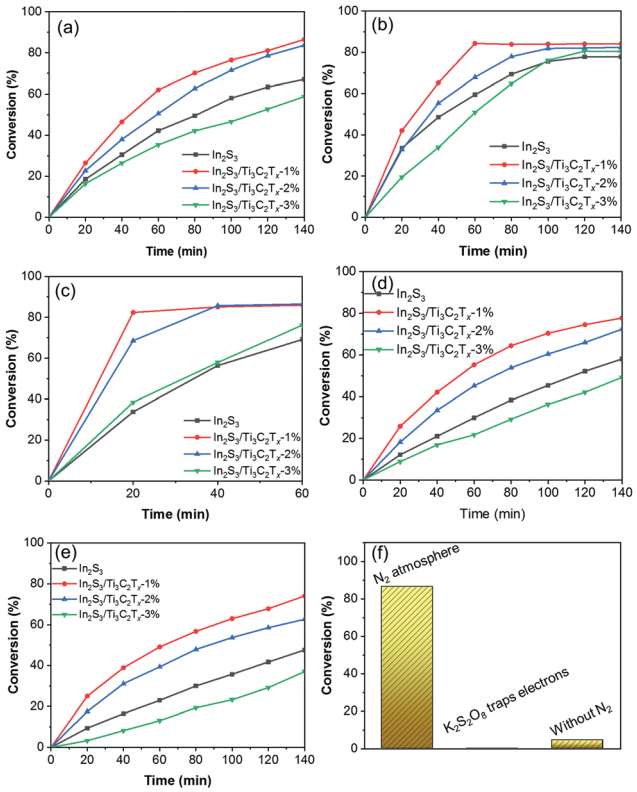

Fig. 3 Photocatalytic selective hydrogenation of 4-NA (a), 4-nitrotoluene (b), 1-chloro-4-nitrobenzene (c), 4-nitroanisole (d), and 4-nitrophenol (e) over In_2S_3 and $In_2S_3/Ti_3C_2T_x$ composites under visible light irradiation. Control experiments for the photocatalytic selective hydrogenation of 4-NA over $In_2S_3/Ti_3C_2T_x$-1% (f).

nitroaromatic compounds with different substituent groups (4-nitrotoluene, 1-chloro-4-nitrobenzene, 4-nitroanisole and 4-nitrophenol), as shown in Fig. 3b–e. In order to investigate the mechanism for the photocatalytic reduction of 4-NA, controlled experiment with the addition of $K_2S_2O_8$ as a scavenger for photogenerated electrons has been conducted. As shown in Fig. 3f, photocatalytic activity of the $In_2S_3/Ti_3C_2T_x$-1% composite is strongly inhibited, and almost no conversion of 4-NA has been observed. The results give direct evidence to prove that the photocatalytic reduction of 4-NA is driven by photogenerated electrons. When N_2 injection was cut off, the photocatalytic activities of $In_2S_3/Ti_3C_2T_x$-1% decreased significantly and the conversion of 4-NA was only 4.4%, illustrating that the inert atmosphere is indispensable for the conversion of 4-NA over the $In_2S_3/Ti_3C_2T_x$ composite. In order to detect whether $Ti_3C_2T_x$ in the $In_2S_3/Ti_3C_2T_x$ composite has been oxidized during photocatalysis, XPS analysis of the $In_2S_3/Ti_3C_2T_x$ composite after the photocatalytic activity test has been conducted. As shown in Fig. S8 (ESI†), the contents of the Ti (IV)–O bond for $In_2S_3/Ti_3C_2T_x$ before and after photocatalytic tests are 17.0% and 17.8%, respectively, which clearly unravels the stability of $Ti_3C_2T_x$.

To investigate the underlying reasons for the improved photocatalytic activity of $In_2S_3/Ti_3C_2T_x$-1% compared to bare In_2S_3, the surface areas of In_2S_3 and $In_2S_3/Ti_3C_2T_x$-1% have been revealed by the nitrogen (N_2) adsorption–desorption measurements. However, as reflected in Fig. S9 (ESI†), the specific surface area of $In_2S_3/Ti_3C_2T_x$-1% (49.6 $m^2\ g^{-1}$) is smaller than bare In_2S_3, which can be attributed to the stacking of nanosheets.[13] This result clearly demonstrates that the surface area is not the key factor determining the photoactivity in the current system. The separation of photogenerated electron–hole pairs is a significant step in photocatalysis,[36] hence a set of electrochemical, photoelectrochemical and photoluminescence (PL) measurements have been performed over In_2S_3 and $In_2S_3/Ti_3C_2T_x$-1%. The cyclic voltammograms show clear anodic and cathodic peaks of $K_3[Fe(CN)_6]/K_4[Fe(CN)_6]$ over bare In_2S_3 and $In_2S_3/Ti_3C_2T_x$-1% (Fig. 4a). A higher current density and smaller overpotential are observed in the $In_2S_3/Ti_3C_2T_x$-1% electrode, which corresponds to the improved electron transfer rate as compared to bare In_2S_3. Besides, as evidenced by the Nyquist plots displayed in Fig. 4b, the $In_2S_3/Ti_3C_2T_x$-1% electrode exhibits a smaller high-frequency semicircle as compared to bare In_2S_3. This result indicates that the lower charge transfer resistance in the $In_2S_3/Ti_3C_2T_x$-1% composite favors faster transport and more effective separation of photo-generated charges carriers.[37] As shown in the photoluminescence (PL) spectra in Fig. 4c, bare In_2S_3 exhibits a broad peak at around 700 nm, while the PL intensity of the $In_2S_3/Ti_3C_2T_x$-1% composite decreases, suggesting that the introduction of $Ti_3C_2T_x$ effectively inhibits the recombination of photogenerated electron–hole pairs. The photoelectron lifetime of two samples has been compared through an open circuit photovoltage (OCP) decay technique under visible light irradiation (Fig. S10, ESI†). It is distinctly seen that from Fig. 4d, the calculated photoelectron lifetime as a function of V_{oc} follows the order of $In_2S_3/Ti_3C_2T_x$-1% > In_2S_3, further demonstrating that the introduction of $Ti_3C_2T_x$ nanosheets can effectively restrain the recombination of photo-induced electron–hole pairs and prolongs the lifetime of charge carriers. In combination with the electrochemical, photoelectrochemical and PL results, it can also be

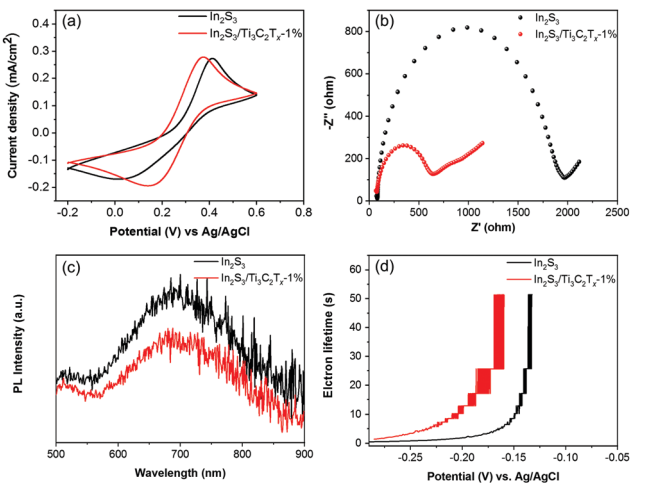

Fig. 4 Cyclic voltammograms (CV) (a), electrochemical impedance spectroscopy (EIS) results (b), photoluminescence (PL) spectra (c), and electron lifetime (d) of In_2S_3 and $In_2S_3/Ti_3C_2T_x$-1%.

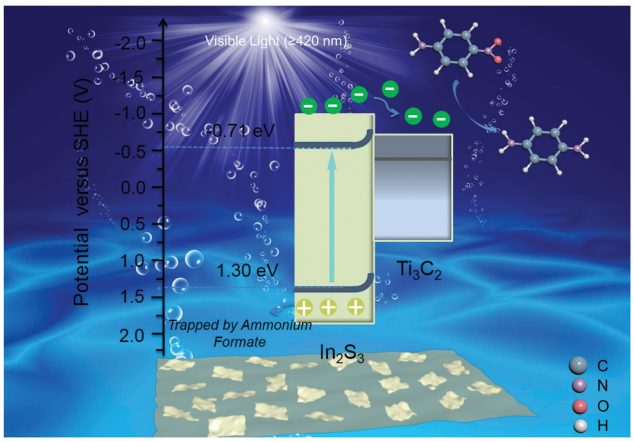

Fig. 5 Illustration of the proposed reaction mechanism for the photocatalytic selective reduction of nitroaromatic compounds over In_2S_3/$Ti_3C_2T_x$ composites.

concluded that the 2D/2D In_2S_3/$Ti_3C_2T_x$ heterostructures play a superior role in enhancing the separation and transfer of photogenerated electrons, thereby resulting in the improved photoactivity of the In_2S_3/$Ti_3C_2T_x$-1% composite as compared to bare In_2S_3.

As photogenerated electrons are the active species for the reduction of nitroaromatic compounds as aforementioned, the band positions of In_2S_3 have been calculated to investigate the transfer progress of photogenerated electrons upon visible light irradiation. According to the Kubelka–Munk function plots obtained by DRS spectral transformation (Fig. S5, ESI†), the band gap (E_g) of In_2S_3 has been measured as 2.01 eV (Fig. S11a, ESI†). Besides, the Mott–Schottky result shown in Fig. S11c (ESI†) suggests that the flat-band potential of In_2S_3 is −0.62 V (*vs.* Ag/AgCl). As shown in Fig. S11b (ESI†), the valence band of In_2S_3 is measured to be 1.30 eV, and then the conduction band is calculated as −0.71 eV according to $E_{VB} = E_{CB} + E_g$.

In light of the above results, a possible mechanism for the photocatalytic reduction of the nitroaromatic compounds has been proposed. As illustrated in Fig. 5, under visible light irradiation ($\lambda \geq 420$ nm), the electrons are photoexcited from the valence band (VB) to the conduction band (CB) of In_2S_3 in the In_2S_3/$Ti_3C_2T_x$ composites, during which holes in the VB are created. Because $Ti_3C_2T_x$ has a more positive Fermi level (E_f) than the E_{CB} of In_2S_3, photoexcited electrons migrate rapidly from the CB of In_2S_3 to $Ti_3C_2T_x$, which inhabits the recombination with holes, thus promoting the reduction reaction of nitroaromatic compounds. Simultaneously, holes in the VB are captured by ammonium formate, which restrains the oxidation of nitroaromatic compounds and their reduction products. Notably, an anaerobic atmosphere is critical to reduce the competition reaction of oxygen reduction to ensure the desirable hydrogenation of nitroaromatic compounds. The improved photocatalytic activity of In_2S_3/$Ti_3C_2T_x$-1% can be interpreted by the favorable active site exposure in the 2D/2D heterostructures and the "electron sink" effect of $Ti_3C_2T_x$ nanosheets, which can boost the transport and separation of photogenerated charge carriers.

4. Conclusions

In conclusion, In_2S_3/$Ti_3C_2T_x$ composites have been fabricated through a low temperature refluxing method. Interestingly, the introduction of $Ti_3C_2T_x$ nanosheets leads to the controlled growth of In_2S_3 nanoflakes, which results from the steric hindrance from adjacent seeds to hinder the in-plane direction growth. $Ti_3C_2T_x$ nanosheets also serve as an efficient co-catalyst for further promoting the separation and transfer of photogenerated charge carriers from In_2S_3 under visible light irradiation. As a result, the 2D heterostructured In_2S_3/$Ti_3C_2T_x$ composites exhibit improved photocatalytic activity compared to bare In_2S_3 toward the hydrogenation reduction of nitroaromatic compounds under visible light irradiation. This work provides a new vision for making better use of the rich surface properties and metal conductivity of $Ti_3C_2T_x$ for the construction of 2D heterostructured photocatalysts.

Author contributions

Yisong Zhu: methodology, conceptualization, investigation, formal analysis, writing – original draft. Guanshun Xie: resources, investigation, visualization. Guohao Li: resources. Fei Song: resources. Changqiang Yu: resources. Zhenjun Wu: resources. Xiuqiang Xie: project administration, supervision, writing – review & editing. Nan Zhang: project administration, supervision, writing – review & editing.

Conflicts of interest

There are no conflicts to decalre.

Acknowledgements

This work was supported by the National Natural Science Foundation of China (52071137, 51977071, 51802040, 218 02020) and the Natural Science Foundation of Hunan Province (2020JJ3004, 2020JJ4192). N. Z. and X. X. also acknowledge the financial support of the Fundamental Research Funds for the Central Universities.

References

1 D. Zhao and C. Cai, Layered Ti_3C_2 MXene modified two-dimensional Bi_2WO_6 composites with enhanced visible light photocatalytic performance, *Mater. Chem. Front.*, 2019, **3**, 2521–2528.

2 Y. Li, S. Yang, Z. Liang, Y. Xue, H. Cui and J. Tian, 1T-MoS_2 nanopatch/Ti_3C_2 MXene/TiO_2 nanosheet hybrids for efficient photocatalytic hydrogen evolution, *Mater. Chem. Front.*, 2019, **3**, 2673–2680.

3 C. Liu, Y. Feng, Z. Han, Y. Sun, X. Wang, Q. Zhang and Z. Zou, Z-scheme N-doped $K_4Nb_6O_{17}$/*g*-C_3N_4 heterojunction with superior visible-light-driven photocatalytic activity for organic pollutant removal and hydrogen production, *Chin. J. Catal.*, 2021, **42**, 164–174.

4 N. Zhang, M.-Q. Yang, S. Liu, Y. Sun and Y.-J. Xu, Waltzing with the Versatile Platform of Graphene to Synthesize Composite Photocatalysts, *Chem. Soc. Rev.*, 2015, **115**, 10307–10377.

5 J. D. Xiao, L. Han, J. Luo, S. H. Yu and H. L. Jiang, Integration of Plasmonic Effects and Schottky Junctions into Metal-Organic Framework Composites: Steering Charge Flow for Enhanced Visible-Light Photocatalysis, *Angew. Chem., Int. Ed.*, 2018, **57**, 1103–1107.

6 G. Zhao, Y. Sun, W. Zhou, X. Wang, K. Chang, G. Liu, H. Liu, T. Kako and J. Ye, Superior Photocatalytic H_2 Production with Cocatalytic Co/Ni Species Anchored on Sulfide Semiconductor, *Adv. Mater.*, 2017, **29**, 1703258.

7 M. Wang, L. Cai, Y. Wang, F. Zhou, K. Xu, X. Tao and Y. Chai, Graphene-Draped Semiconductors for Enhanced Photocorrosion Resistance and Photocatalytic Properties, *J. Am. Chem. Soc.*, 2017, **139**, 4144–4151.

8 Y. Zhang, Z. Chen, S. Liu and Y.-J. Xu, Size effect induced activity enhancement and anti-photocorrosion of reduced graphene oxide/ZnO composites for degradation of organic dyes and reduction of Cr(VI) in water, *Appl. Catal., B*, 2013, **140–141**, 598–607.

9 C. Liu, H. Zhu, Y. Zhu, P. Dong, H. Hou, Q. Xu, X. Chen, X. Xi and W. Hou, Ordered layered N-doped $KTiNbO_5$/g-C_3N_4 heterojunction with enhanced visible light photocatalytic activity, *Appl. Catal., B*, 2018, **228**, 54–63.

10 Y. Qin, H. Li, J. Lu, Y. Feng, F. Meng, C. Ma, Y. Yan and M. Meng, Synergy between van der Waals heterojunction and vacancy in $ZnIn_2S_4$/g-C_3N_4 2D/2D photocatalysts for enhanced photocatalytic hydrogen evolution, *Appl. Catal., B*, 2020, **277**, 119254.

11 Y. Li, Y. Liu, D. Xing, J. Wang, L. Zheng, Z. Wang, P. Wang, Z. Zheng, H. Cheng, Y. Dai and B. Huang, 2D/2D heterostructure of ultrathin $BiVO_4$/Ti_3C_2 nanosheets for photocatalytic overall Water splitting, *Appl. Catal., B*, 2021, **285**, 119855.

12 J. Xiao, X. Li, K. Tang, D. Wang, M. Long, H. Gao, W. Chen, C. Liu, H. Liu and G. Wang, Recent progress of emerging cathode materials for sodium ion batteries, *Mater. Chem. Front.*, 2021, **5**, 3735–3764.

13 S. W. Cao, B. J. Shen, T. Tong, J. W. Fu and J. G. Yu, 2D/2D Heterojunction of Ultrathin MXene/Bi_2WO_6 Nanosheets for Improved Photocatalytic CO_2 Reduction, *Adv. Funct. Mater.*, 2018, **28**, 1800136.

14 Y. Wu, H. Wang, W. Tu, Y. Liu, S. Wu, Y. Z. Tan and J. W. Chew, Construction of hierarchical 2D-2D $Zn_3In_2S_6$/fluorinated polymeric carbon nitride nanosheets photocatalyst for boosting photocatalytic degradation and hydrogen production performance, *Appl. Catal., B*, 2018, **233**, 58–69.

15 Y. Ao, K. Wang, P. Wang, C. Wang and J. Hou, Synthesis of novel 2D-2D p–n heterojunction BiOBr/$La_2Ti_2O_7$ composite photocatalyst with enhanced photocatalytic performance under both UV and visible light irradiation, *Appl. Catal., B*, 2016, **194**, 157–168.

16 Z. Zhang, J. Huang, M. Zhang, Q. Yuan and B. Dong, Ultrathin hexagonal SnS_2 nanosheets coupled with g-C_3N_4 nanosheets as 2D/2D heterojunction photocatalysts toward high photocatalytic activity, *Appl. Catal., B*, 2015, **163**, 298–305.

17 W.-J. Ong, L.-L. Tan, S.-P. Chai, S.-T. Yong and A. R. Mohamed, Surface charge modification via protonation of graphitic carbon nitride (g-C_3N_4) for electrostatic self-assembly construction of 2D/2D reduced graphene oxide (rGO)/g-C_3N_4 nanostructures toward enhanced photocatalytic reduction of carbon dioxide to methane, *Nano Energy*, 2015, **13**, 757–770.

18 J. Huo, L. Lu, Z. Shen, H. Gao and H. Liu, Rational Design of CoNi Alloy and Atomic Co/Ni comPosite as an Efficient Electrocatalyst, *Surf. Innovations*, 2021, **9**, 37–48.

19 M. Naguib, M. Kurtoglu, V. Presser, J. Lu, J. Niu, M. Heon, L. Hultman, Y. Gogotsi and M. W. Barsoum, Two-Dimensional Nanocrystals: Two-Dimensional Nanocrystals Produced by Exfoliation of Ti_3AlC_2, *Adv. Mater.*, 2011, **23**, 4207.

20 G. Zuo, Y. Wang, W. L. Teo, A. Xie, Y. Guo, Y. Dai, W. Zhou, D. Jana, Q. Xian, W. Dong and Y. Zhao, Ultrathin $ZnIn_2S_4$ Nanosheets Anchored on Ti_3C_2TX MXene for Photocatalytic H_2 Evolution, *Angew. Chem., Int. Ed.*, 2020, **59**, 11287–11292.

21 M. Naguib, V. N. Mochalin, M. W. Barsoum and Y. Gogotsi, Two-Dimensional Materials: 25th Anniversary Article: MXenes: A New Family of Two-Dimensional Materials (Adv. Mater. 7/2014), *Adv. Mater.*, 2014, **26**, 982.

22 O. Mashtalir, K. M. Cook, V. N. Mochalin, M. Crowe, M. W. Barsoum and Y. Gogotsi, Dye adsorption and decomposition on two-dimensional titanium carbide in aqueous media, *J. Mater. Chem. A*, 2014, **2**, 14334–14338.

23 H. Wang, R. Peng, Z. D. Hood, M. Naguib, S. P. Adhikari and Z. Wu, Titania Composites with 2D Transition Metal Carbides as Photocatalysts for Hydrogen Production under Visible-Light Irradiation, *ChemSusChem*, 2016, **9**, 1490–1497.

24 J. Low, L. Zhang, T. Tong, B. Shen and J. Yu, TiO_2/MXene Ti_3C_2 composite with excellent photocatalytic CO_2 reduction activity, *J. Catal.*, 2018, **361**, 255–266.

25 Q. Liu, L. Ai and J. Jiang, MXene-derived TiO_2@C/g-C_3N_4 heterojunctions for highly efficient nitrogen photofixation, *J. Mater. Chem. A*, 2018, **6**, 4102–4110.

26 X. Q. Xie and N. Zhang, Positioning MXenes in the Photocatalysis Landscape: Competitiveness, Challenges, and Future Perspectives, *Adv. Funct. Mater.*, 2020, **30**, 2002528.

27 X. Q. Xie, N. Zhang, Z. R. Tang, M. Anpo and Y. J. Xu, $Ti_3C_2T_x$ MXene as a Janus cocatalyst for concurrent promoted photoactivity and inhibited photocorrosion, *Appl. Catal., B*, 2018, **237**, 43–49.

28 Z. Zeng, Y. Yan, J. Chen, P. Zan, Q. Tian and P. Chen, Boosting the Photocatalytic Ability of Cu_2O Nanowires for CO_2 Conversion by MXene Quantum Dots, *Adv. Funct. Mater.*, 2019, 29.

29 Y. J. Xu, S. Wang, J. Yang, B. Han, R. Nie, J. X. Wang, J. G. Wang and H. W. Jing, *In situ* grown nanocrystal TiO_2 on 2D Ti_3C_2 nanosheets for artificial photosynthesis of chemical fuels, *Nano Energy*, 2018, **51**, 442–450.

30 H. Lin and X. Wang, Epitaxy of Radial High-Energy-Facetted Ultrathin TiO_2 Nanosheets onto Nanowires for Enhanced Photoreactivities, *Adv. Funct. Mater.*, 2016, **26**, 1580–1589.
31 Y. Xiong, Y. Xie, G. Du, X. Tian and Y. Qian, A Novel *in Situ* Oxidization–Sulfidation Growth Route *via* self-Purification Process to β-In_2S_3 Dendrites, *J. Solid State Chem.*, 2002, **166**, 336–340.
32 Y. Chen, X. Xie, X. Xin, Z. R. Tang and Y. J. Xu, $Ti_3C_2T_x$-Based Three-Dimensional Hydrogel by a Graphene Oxide-Assisted Self-Convergence Process for Enhanced Photoredox Catalysis, *ACS Nano*, 2019, **13**, 295–304.
33 W. Huang, L. Gan, H. Yang, N. Zhou, R. Wang, W. Wu, H. Li, Y. Ma, H. Zeng and T. Zhai, Controlled Synthesis of Ultrathin 2D β-In_2S_3 with Broadband Photoresponse by Chemical Vapor Deposition, *Adv. Funct. Mater.*, 2017, **27**, 1702448.
34 Y.-S. Xie, L. Yuan, N. Zhang and Y.-J. Xu, Light-tuned switching of charge transfer channel for simultaneously boosted photoactivity and stability, *Appl. Catal., B*, 2018, **238**, 19–26.
35 X. Xie, C. Chen, N. Zhang, Z.-R. Tang, J. Jiang and Y.-J. Xu, Microstructure and surface control of MXene films for water purification, *Nat. Sustainability*, 2019, **2**, 856–862.
36 N. Zhang, C. Han, X. Fu and Y.-J. Xu, Function-Oriented Engineering of Metal-Based Nanohybrids for Photoredox Catalysis: Exerting Plasmonic Effect and Beyond, *Chem*, 2018, **4**, 1832–1861.
37 J.-Y. Li, Y.-H. Li, F. Zhang, Z.-R. Tang and Y.-J. Xu, Visible-light-driven integrated organic synthesis and hydrogen evolution over 1D/2D CdS-$Ti_3C_2T_x$ MXene composites, *Appl. Catal., B*, 2020, **269**, 118783.

